scientific reports

OPEN

Study on the durability and mechanical properties of carbon fiber reinforced concrete for shaft lining under chloride salt freeze–thaw coupling environment

Gejun Tong[1✉], Jiaping Xiao[1], Zehong Sun[1], Jianyong Pang[2] & Ruiqi Zheng[2]

Deep mining shaft lining concrete structures face durability challenges due to long-term exposure to complex environments. This study investigates the mechanical properties and degradation mechanisms of carbon fiber reinforced concrete (CFRC) under combined chloride erosion and freeze–thaw cycles. Tests were conducted to compare CFRC with ordinary concrete (OC), focusing on static and dynamic mechanical performance. Results indicate that CFRC with an optimal carbon fiber content exhibits significantly improved comprehensive properties, including enhanced compressive and splitting tensile strength. Although concrete mechanical properties generally decline with increasing freeze–thaw cycles, CFRC demonstrates superior resistance to chloride penetration and freeze–thaw damage compared to OC. The findings confirm carbon fiber's effectiveness in mitigating deterioration in harsh environmental conditions.

Currently, concrete is widely used in mine construction due to its good economy, strong plasticity, excellent bond properties, and high safety[1,2]. However, the deep freezing process adversely affects concrete structures, reducing their service life. Maintenance and reconstruction costs underground are extremely high. Therefore, to extend the service life of underground structures, research on the impact of complex environments on concrete durability and the need for treatment measures is becoming increasingly urgent[3–5].

The impact of deep environments on concrete durability can be primarily summarized into three aspects: the chemical interaction between groundwater and cement hydration products, mechanical actions during operation, and freeze–thaw and wet-dry cycles[6]. Chloride ions, sulfate particles, and magnesium ions in groundwater react with concrete components, causing partial erosion and structural deterioration. Among these, chloride ions are the primary cause of structural corrosion[7,8].

Suryavanshi et al.[9] analyzed the formation mechanism of Friedel's salt in concrete in NaCl solution based on void solution, and found that it was mainly formed by adsorption mechanism and anion exchange mechanism. Farnam et al.[6] found that ordinary Portland cement undergoes a destructive reaction with NaCl, while calcium silicate-based cement does not react chemically with NaCl. However, both ordinary Portland cement and calcium silicate-based cement react chemically with $MgCl_2$. Since the migration of chloride ions to the steel surface can lead to steel corrosion, Qingfeng et al.[7] studied chloride ion transport in various ionic environments. They established a multi-ion coupling transport model for chloride and other ions, discovering that calcium leaching significantly affects chloride ion transport. The multi-ion coupling effect promotes calcium leaching in the early stages but slows it down in the later stages. From the perspective of chemical erosion, the performance deterioration of ordinary Portland cement concrete in seawater is mainly due to the susceptibility of calcium hydroxide to sulfate attack[10]. Nicola et al.[11] simulated the chemical erosion of concrete in unsaturated or saturated sulfate solutions. By using a simplified diffusion model, they calculated the water content and expansion products of the cement paste, thereby determining the stress state and degradation of the concrete[12].

[1]Huainan Vocational Technical College, Huainan 232001, Anhui Province, China. [2]School of Civil Engineering and Architecture, Anhui University of Science and Technology, Huainan 232001, Anhui Province, China. ✉email: 1513667827@qq.com

Concrete is a porous, brittle material prone to brittle fracture and exhibits poor impact resistance. Its critical failure characteristic is the near-complete loss of load-bearing capacity once damaged, while its operational performance involves exposure to impact loading[13]. Shaojie et al.[10] conducted impact tests on concrete specimens soaked in sodium chloride solution using a split Hopkinson pressure bar test system. They found that as the number of impacts increased, the dynamic compressive strength of the concrete gradually decreased, and the specimen fractures increased accordingly. Additionally, freeze–thaw and wet-dry cycles also affect concrete deterioration[14–17].

To address the adverse effects of deep complex environments on concrete durability, the primary remediation measures are classified into two categories: modification of internal composition and application of surface coatings[18,19]. Altering internal components involves replacing or adding new materials to the concrete mix[20,21]. Sylvia et al.[22] found that using natural volcanic ash, fly ash, and ground granulated blast-furnace slag as partial replacements for limestone cement can delay and inhibit sulfate attack, thereby improving durability. Fly ash effectively enhances the sulfate resistance of limestone concrete, whereas natural volcanic ash shows less improvement. Deveshan et al.[19] used finer metakaolin to replace ordinary Portland cement, resulting in lower porosity, improved microstructure, and better durability of metakaolin concrete. Bo et al.[20] incorporated ground granulated blast-furnace slag into coal gangue-based geopolymer concrete, enhancing the material's strength and density. An appropriate amount of slag can more than double the freeze–thaw resistance of the material, with higher slag content reducing porosity.

While replacing and adding cementitious materials can improve concrete density, they do not address the issue of microcracks within the concrete, which can lead to severe erosion at the crack sites[23,24]. To enhance impact resistance and reduce cracking, researchers have incorporated fibers into concrete, with polypropylene and basalt fibers being the most commonly used[25–28]. Additionally, carbon fiber, a high-performance fiber with high elastic modulus, fatigue resistance, corrosion resistance, and low density, is widely used in aerospace, aviation, and sports equipment but less so in construction. Compared to polypropylene and basalt fibers, carbon fiber offers higher strength and better corrosion resistance. Carbon fiber also has good electrical conductivity, which can effectively detect damage characteristics when added to concrete. Additionally, carbon fiber, a high-performance material known for its high elastic modulus, fatigue resistance, corrosion resistance, and low density, has also been introduced into construction by researchers. Kavitha et al.[29] finds through experiments that adding carbon fiber to concrete is more effective than adding basalt fiber in enhancing its tensile strength, flexural strength, and modulus of elasticity. Deng et al.'s[30] three-point bending tests revealed that pre-cyclic loading reduces the fracture parameters of both carbon fiber-reinforced concrete and plain concrete. However, carbon fiber-reinforced concrete can withstand a higher stress threshold, and its critical effective crack length is significantly greater than that of plain concrete. Wei et al.[31] experimentally investigated the feasibility of using chopped carbon fiber waste to inhibit steel corrosion in reinforced concrete structures. After 360 days of sustained loading, it was found that the corrosion rate of beam specimens incorporating chopped carbon fiber was reduced by up to approximately 20% compared to the control group. Li et al.'s[32] study evaluated the static and dynamic mechanical properties of three types of fiber-reinforced concrete: carbon fiber-reinforced concrete (CFRC), Kevlar fiber-reinforced concrete (KFRC), and their hybrid (HFRC). The results demonstrated significant improvements in the mechanical performance of all fiber-reinforced concrete types. Specifically, the HFRC made with 24-mm carbon and Kevlar fibers exhibited the most outstanding performance in both static strength (compressive, flexural, and splitting tensile strength) and impact resistance. However, few studies have concurrently investigated both the static and dynamic properties of carbon fiber reinforced concrete under complex environmental conditions.

This paper investigates the comprehensive performance of carbon fiber reinforced concrete in deep complex mine environments. After optimizing the mix proportions of different carbon fiber content concretes, mechanical tests were conducted to identify the optimal performance carbon fiber concrete. Further research was carried out on the degradation performance of carbon fiber concrete under chloride salt and freeze–thaw cycles, revealing the static and dynamic load degradation mechanisms of carbon fiber concrete in complex environments. This has significant engineering implications for improving the service durability of concrete.

Materials and methods
Materials
The cement used is P·O.42.5 grade ordinary Portland cement, with its chemical composition and content shown in Table 1, and main performance indicators listed in Table 2. The carbon fiber used is straight type, with key performance parameters provided in Table 3, and its appearance depicted in Fig. 1. The sand used for the experiment is natural ultra-fine quartz sand, with a silicon content of 97.89%, an apparent density of 2510 kg/m^3, and a fineness modulus of 2.67. The coarse aggregate used is continuously graded pebble with an apparent density of 2609 kg/m^3, particle sizes ranging from 5 to 31.5 mm, a bulk density of 1575 kg/m^3, and a mud content of 1.1%. Ordinary tap water was used. The water reducer employed is PCA-Ⅰ type high-efficiency water reducing agent, with specific performance parameters shown in Table 4.

Component	CaO	SiO$_2$	Fe$_2$O$_3$	Al$_2$O$_3$	MgO	SO$_3$	Na$_2$O	K$_2$O	Other
Content (%)	59.33	18.74	5.16	4.93	3.92	2.62	0.30	0.10	4.9

Table 1. Chemical composition and content of cement.

Model	Density/(kg m⁻³)	Setting time (min)		Compressive strength (MPa)		Flexural strength (MPa)	
		Initial set	Final set	3d	28d	3d	28d
42.5	2900	175	235	≥ 26.5	≥ 48.5	≥ 6.0	≥ 8.5

Table 2. Cement property parameter.

Density (kg m⁻³)	Tensile strength (MPa)	Length (mm)	Carbon content (%)	Monofilament diameter (μm)	Tensile modulus (GPa)
1800	3450	3	95	7	230

Table 3. Carbon fiber parameter.

Fig. 1. 20 mm chopped carbon fiber.

Water reduction rate (%)	Bleeding rate (%)	Gas content (%)	Initial set (min)	Final set (min)
30	40	2	35	50

Table 4. The performance index of water reducing agent.

Group	Cement	Pebble	sand	Water	Carbon fiber	Water Reducing agent
C_0	361	650	1360	145	0	3.61
$C_{0.2}$	361	650	1360	145	3.6	3.61
$C_{0.4}$	361	650	1360	145	7.2	3.61
$C_{0.6}$	361	650	1360	145	10.8	3.61
$C_{0.8}$	361	650	1360	145	14.4	3.61

Table 5. Mix ratio of carbon fiber concrete specimen (kg m⁻³).

Specimen preparation

Concrete specimens were prepared with carbon fiber contents (ω_c) of 0%, 0.2%, 0.4%, 0.6%, and 0.8%. The specific mix proportions are provided in Table 5. Cement, pebble, and sand were sequentially added into the mixer and thoroughly mixed. The carbon fibers were then gradually added in small increments, and the mixture was stirred for 3 min. Afterward, water was added, and the mixture was wet-mixed for an additional 4 min. The resulting mixture was poured into pre-lubricated 100mmx100mmx100mm cubic molds. These molds were placed on a vibration table for compaction and molding. The surface was then smoothed with a trowel, and the vibration was stopped. The concrete specimens were covered with plastic wrap and allowed to set for 24 h before demolding. The specimens were then cured under standard conditions for 28 days. The experimental procedure is illustrated in Fig. 2.

Experimental design

According to *Standard for Test Methods of Concrete Physical and Mechanical Properties (GBT50081-2019)*[33], the static mechanical properties of the cured specimens were tested. As shown in Fig. 2, each test group underwent
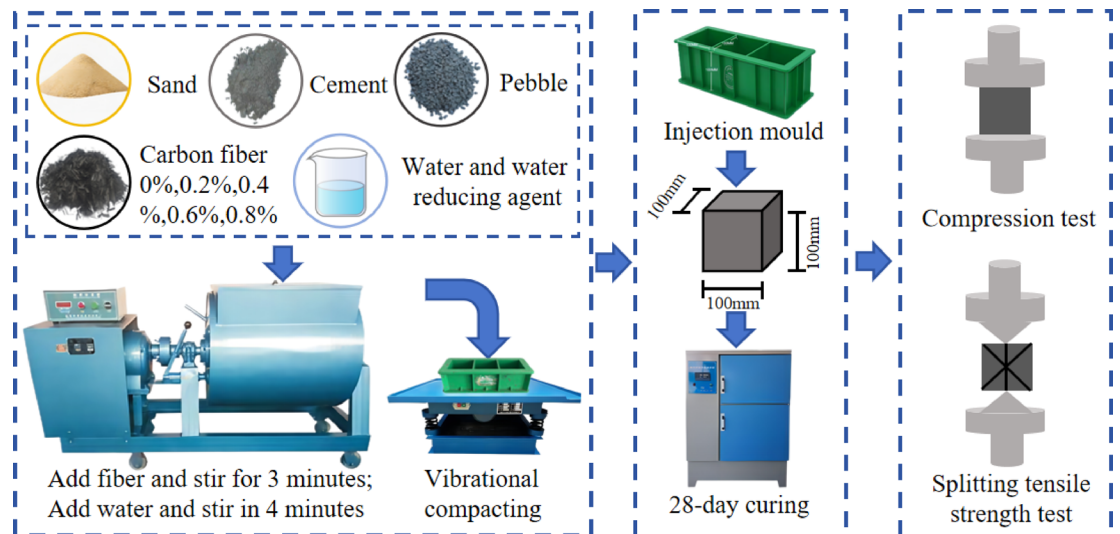
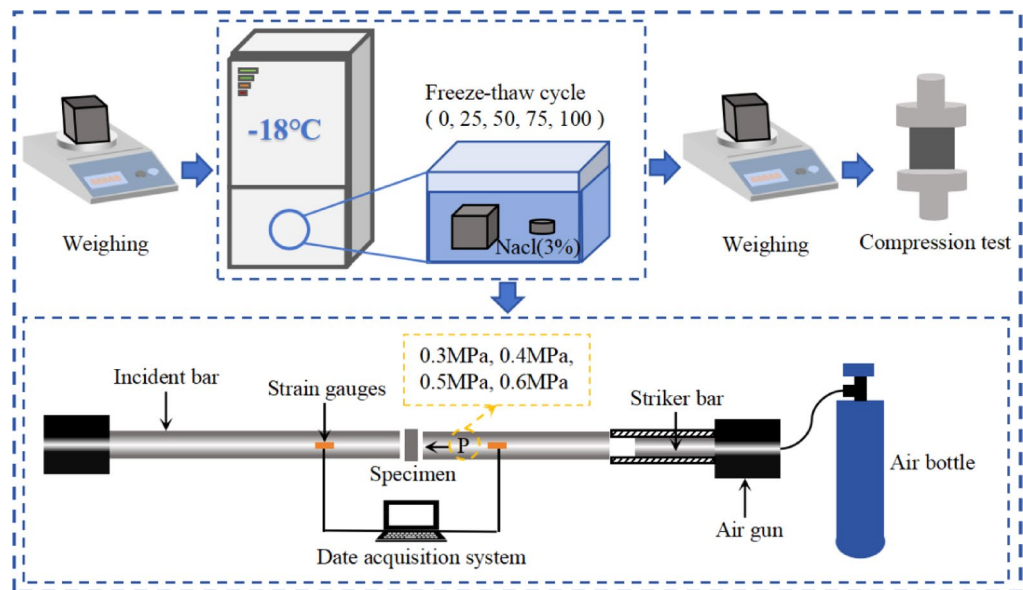**Fig. 2**. Sample preparation and test flow chart.

Fig. 3. Freeze–thaw cycle and test flow chart.

three parallel tests to prevent experimental errors caused by data dispersion, and the optimal mix proportion was comprehensively selected.

Using the optimal mix proportion, 100 mm × 100 mm × 100 mm cubic specimens and 74 mm × 25 mm cylindrical specimens were prepared and tested according to *Standard for Test Methods of Long-term Performance and Durability of Ordinary Concrete (GBT50082-2009)*[34]. To simulate a chloride environment, the specimens were placed in a 3% NaCl solution, ensuring the water level was above the top surface of the specimens. The freeze–thaw cycles(n) were set to 0, 25, 50, 75, and 100 cycles. The freezing period began when the equipment temperature dropped to − 18 °C, with a freezing time of 6 h and a melting time of 6 h, constituting one complete freeze–thaw cycle. The static and dynamic mechanical properties of the specimens were tested after different numbers of freeze–thaw cycles. The dynamic test was conducted with four levels of impact air pressure: 0.3 MPa, 0.4 MPa, 0.5 MPa, and 0.6 MPa. Each air pressure level was tested three times per specimen group. Before the tests, a small amount of petroleum jelly was applied to both ends of the concrete specimens to reduce friction interference. The experimental procedure is illustrated in Fig. 3. This experiment employed a split Hopkinson pressure bar (SHPB) system with a bar diameter of 74 mm. The bars were made of high-strength maraging steel, with an elastic modulus of 190 GPa, a density of 8100 kg/m^3, and a measured elastic wave velocity of 4840 m/s. The lengths of the incident and transmission bars were 2400 mm and 1200 mm, respectively. The projectile was a flat-ended cylinder with a length of 200 mm, propelled by regulated gas pressure. Its impact velocity, measured
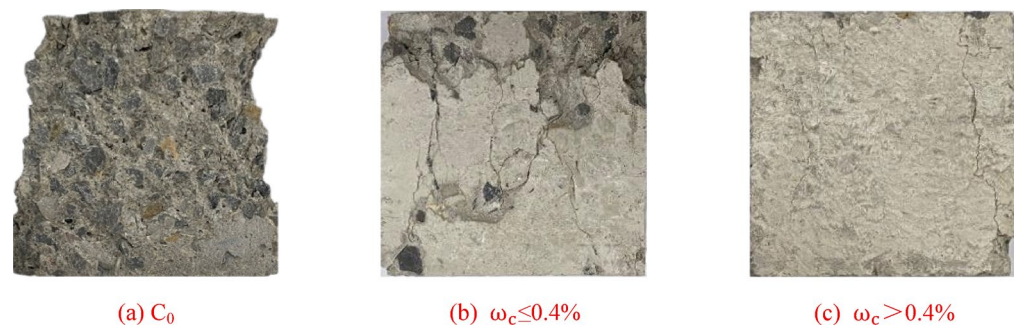
(a) C$_0$ (b) $\omega_c \leq 0.4\%$ (c) $\omega_c > 0.4\%$

Fig. 4. Failure modes of concrete specimens under compressive tests with different carbon fiber contents.

Group	C$_0$	C$_{0.2}$	C$_{0.4}$	C$_{0.6}$	C$_{0.8}$
Compressive strength (MPa)	43.456	45.6	49.982	36.928	33.14
Splitting tensile strength (MPa)	4.349	6.146	6.572	6.361	5.454
Slump (mm)	55	50	44	35	21

Table 6. Uniaxial Strength and Slump of concrete specimens.

(a) C$_0$ (b) $\omega_c \leq 0.4\%$ (c) $\omega_c > 0.4\%$
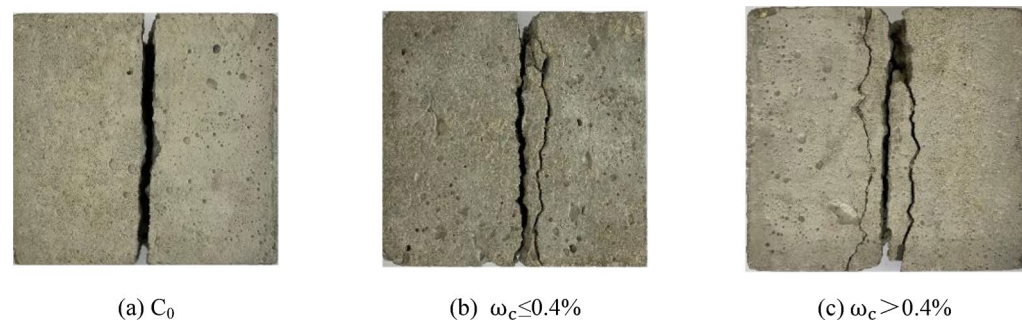
Fig. 5. Failure modes of splitting tensile test of concrete specimens with different carbon fiber contents.

using a laser velocimeter, was 18.5 m/s. Data acquisition was performed using a National Instruments PXIe system with a sampling rate set to 5 MHz.

Results and discussion
Static mechanical properties of carbon fiber reinforced concrete in normal environment
Compressive strength and splitting tensile strength

The final failure modes of concrete specimens with different carbon fiber contents under compression tests are shown in Fig. 4, and the compressive strength results are presented in Table 6. The failure of concrete specimens without carbon fiber was brittle, resulting in thorough destruction with a final hourglass-shaped failure mode. As the fiber content increased, the surface spalling of the specimens decreased during the loading process, and the overall integrity of the concrete specimens improved after loading, exhibiting a "cracked but not scattered" failure mode. This is in contrast to the specimens without carbon fiber, which experienced significant spalling after losing their load-bearing capacity. Compared to ordinary concrete (OC), the compressive strength of specimens increased as the carbon fiber content rose from 0% to 0.4%, although the increase was slight. However, as the carbon fiber content continued to increase beyond 0.4%, the compressive strength began to decline, eventually falling below that of OC, with a relatively high rate of decrease. Specifically, the compressive strength of specimens with 0.2%, 0.4%, 0.6%, and 0.8% carbon fiber content increased by 4.93%, 15.02%, − 15.02%, and − 23.74%, respectively, compared to OC.

Figure 5 shows the final failure modes of the split tensile test specimens of concrete with different carbon fiber contents, and the test results are presented in Table 6. From Fig. 5, it can be observed that the OC specimens exhibit a " Ⅰ " type of fracture with a relatively intact failure surface. When the fiber content is low, the failure surface shows main cracks and branch cracks, with lower integrity compared to OC. With a higher fiber content, the specimens exhibit three clear cracks on the failure surface, indicating lower integrity. The split tensile strength increases first and then decreases with the increase in carbon fiber content, with a significant overall increase compared to OC. Specifically, when the carbon fiber content is 0.2%, 0.4%, 0.6%, and 0.8%,

the tensile strength of the specimens increases by 41.32%, 51.12%, 46.26%, and 25.42% respectively compared to OC. This is because, when the carbon fiber is appropriately mixed, it is uniformly distributed within the specimen, forming an interlaced fiber network, acting as a bridge and transmitting stress, and the carbon fiber itself has excellent tensile properties. However, when the carbon fiber content is too high, the poor dispersion and tendency to agglomerate of the carbon fibers lead to a decrease in the workability of the concrete(Table 6), resulting in a negative impact on the mechanical properties of the concrete.

Strain–stress relation

The uniaxial compressive stress–strain curves of CFRC are shown in Fig. 6. It can be seen from Fig. 6 that the stress–strain curves of concrete specimens in each group under uniaxial compression have similar characteristics, including a densification stage, linear elastic stage, elastoplastic stage, and failure stage. During the densification stage, the internal pores of the specimens are compacted, increasing the density, and the stress–strain curve shows a concave trend. As the stress increases, the specimen enters the stage of elastic deformation, and the curve shows a linear trend. As the loading continues, the specimen begins to exhibit plastic deformation, entering the stage of elastoplastic deformation. With the continuous increase in loading, the stress reaches the ultimate bearing capacity of the specimen, entering the failure stage, where the specimen begins to fail, and the bearing capacity begins to decrease.

Based on the above study, the compressive strength of carbon fiber reinforced concrete (CFRC) manifests as $f_{0.4} > f_{0.2} > f_0 > f_{0.6} > f_{0.8}$, the tensile strength as $R_{m0.4} > R_{m0.6} > R_{m0.2} > R_{m0.8} > R_{m0}$, and the peak strain as $\varepsilon_{0.8} > \varepsilon_{0.4} > \varepsilon_{0.6} > \varepsilon_{0.2} > \varepsilon_0$.

Through the analysis of these strength results, the optimal mix ratio for concrete specimens with different carbon fiber contents is determined based on the maximum compressive strength, appropriate peak strain, and maximum tensile strength. Ultimately, the overall performance of CFRC is optimal when the carbon fiber content is 0.4%.

Deterioration performance of carbon fiber reinforced concrete under the combined action of chloride salt and freeze–thaw

Deterioration characteristics

(1) Apparent deterioration

As the number of freeze–thaw cycles increases, the surface damage of the concrete specimens worsens. The apparent morphology of CFRC and OC specimens after different freeze–thaw cycles is shown in Fig. 7. As shown in Fig. 7a–b, when the freeze–thaw cycles are 25 and 50, the surfaces of the CFRC and OC concrete specimens are smooth, with distinct edges and no obvious damage, but with varying degrees of erosion holes. Furthermore, the degree of erosion and the number of surface holes of the concrete specimens after 50 freeze–thaw cycles are significantly greater than those after 25 freeze–thaw cycles. Starting from 75 freeze–thaw cycles, the surfaces of the concrete specimens begin to show significant spalling. Both the CFRC and OC concrete specimens exhibit varying degrees of surface spalling, and the edges of the concrete specimens also show certain damage and loss. When the number of freeze–thaw cycles reaches 100, the surface spalling of the specimens becomes severe, and even fine aggregates begin to detach, exposing the internal coarse aggregates. These observations indicate that with an increasing number of freeze–thaw cycles, the damage to both CFRC and OC concrete specimens becomes more severe, with the degree of surface damage on the OC specimens being more severe than that on the CFRC specimens.
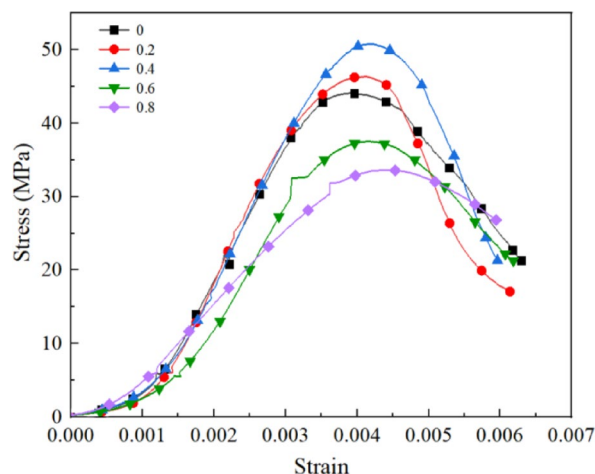
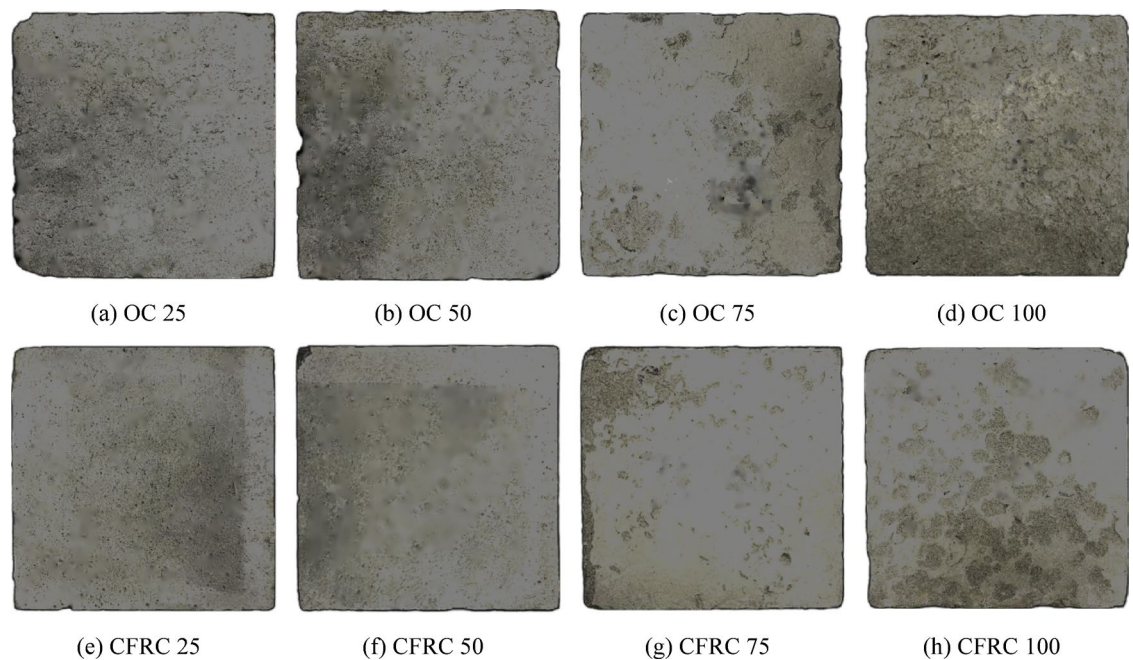(2) Mass variation

Fig. 6. Stress–strain curves of CFRC.

(a) OC 25   (b) OC 50   (c) OC 75   (d) OC 100

(e) CFRC 25   (f) CFRC 50   (g) CFRC 75   (h) CFRC 100

Fig. 7. The apparent morphology of CFRC and OC specimens after different freeze–thaw cycles.
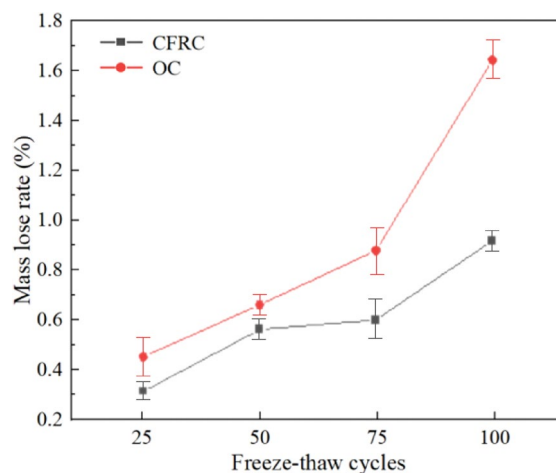

Fig. 8. Mass loss rate of concrete specimens under freeze–thaw cycle.

In order to measure the macroscopic damage indicators after freeze–thaw cycles, the mass loss rate (ΔW) is introduced. The surface cement mortar of the specimens will spall after freeze–thaw treatment, resulting in mass loss. The mass of the specimens before and after freeze–thaw is measured using an electronic scale, and then the mass loss rate of each specimen is calculated based on Eq. (1). The mass before and after freeze–thaw is measured for three specimens in each group, the mass change rate is calculated, and the average is taken as the mass loss rate for that group.

$$\Delta W = \frac{m_0 - m_n}{m_0} \tag{1}$$

In the formula, m_0 represents the mass before freeze–thaw cycling treatment, kg; m_n represents the mass after n cycles of freeze–thaw treatment, kg.

Figure 8 illustrates the variation of mass loss rates of OC and CFRC concrete specimens with freezing–thawing cycles of 25, 50, 75, and 100 cycles.

From Fig. 8, it can be observed that with an increase in the number of freezing–thawing cycles, the mass loss rates of both OC and CFRC concrete specimens continuously increase. At freezing–thawing cycles of 25, 50, 75, and 100 cycles, the mass loss rates of OC concrete specimens are 0.43%, 0.64%, 0.86%, and 1.63% respectively,

while the mass loss rates of CFRC concrete specimens are 0.29%, 0.54%, 0.58%, and 0.90% respectively. When concrete specimens are exposed to chloride solution, the material in the specimens undergoes chemical reactions with chloride ions in the solution, leading to surface cracking and erosion. With an increase in the number of freezing–thawing cycles, the erosion phenomenon on the concrete surface becomes more pronounced. Compared to OC, CFRC exhibits a smaller mass loss rate, attributed to the significant improvement in concrete durability through fiber bridging and pore filling[35,36]. The addition of CF prevents volume expansion during water freezing and effectively resists concrete expansion and crack tension caused by chloride freezing–thawing coupling, thereby suppressing crack occurrence and reducing mass loss.

Static uniaxial compressive strength

Figure 9 shows the static compressive strength of OC and CFRC concrete specimens after different numbers of freezing–thawing cycles in a chloride solution. It can be seen that under the combined action of chloride and freezing–thawing cycles, the trend of change in static compressive strength of CFRC specimens is similar to that of OC specimens, both increasing and then decreasing with an increase in the number of freezing–thawing cycles. After 25, 50, 75, and 100 freezing–thawing cycles, the static compressive strengths of OC are 44.3 MPa, 40.98 MPa, 35.09 MPa, and 34.23 MPa respectively, while the static compressive strengths of CFRC are 50.3 MPa, 47.47 MPa, 42.1 MPa, and 40.73 MPa respectively. Furthermore, the static compressive strength of CFRC is consistently higher than that of OC, indicating that in a chloride solution, the freeze–thaw resistance of CFRC is superior to that of OC.

From Fig. 9, it can be observed that with an increasing number of freezing–thawing cycles, the trend of change in static compressive strength of OC and CFRC is similar. The static compressive strength of both OC and CFRC specimens shows an increasing trend followed by a decrease with an increase in the number of freezing–thawing cycles. Additionally, both OC and CFRC exhibit a significant decrease in static compressive strength at a certain point, after which the decrease in strength tends to stabilize.

In the initial phase of the study, when the number of freezing–thawing cycles is below 25, both ordinary concrete (OC) and carbon fiber reinforced concrete (CFRC) show an increase in dynamic compressive strength. This improvement is attributed to the lower freezing point of the chloride solution, which allows chloride crystals to compress and partially fill the concrete's pores. Moreover, chemical and physical reactions between the chloride solution and concrete enhance the density and static compressive strength of the specimens. However, after 25 cycles, initial cracks in the ordinary concrete begin to expand, leading to a decrease in static compressive strength for both OC and CFRC. The freezing-thaw cycles create conditions that accelerate chloride crystallization and erosion within the concrete, resulting in increased internal pressure and crack formation, which reduces load-bearing capacity. Despite this decline, the static compressive strength of CFRC remains higher than that of OC throughout the tests. The carbon fibers improve the internal compactness of the concrete, creating longer capillary pathways that limit chloride ion ingress. This delays internal reactions and helps prevent the expansion of initial cracks. The findings suggest that carbon fibers effectively mitigate damage from the combined effects of chloride and freezing–thawing cycles on concrete materials.

Due to the initial differences in static compressive strength of OC and CFRC specimens, the magnitude of change in static compressive strength after different numbers of freezing–thawing cycles in a chloride environment also differs. In order to reveal the variation patterns of static compressive strength under different numbers of freezing–thawing cycles for the two groups of concrete, the concept of strength activity index (*SAI*) is introduced to compare the frost resistance of the two types of concrete in Eq. (2).

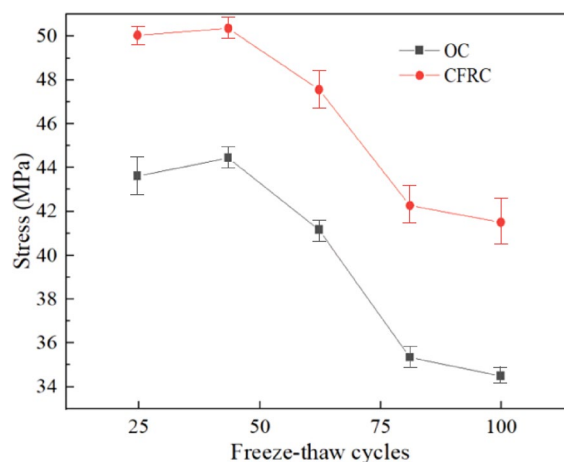$$SAI = \frac{f_n}{f_0} \tag{2}$$

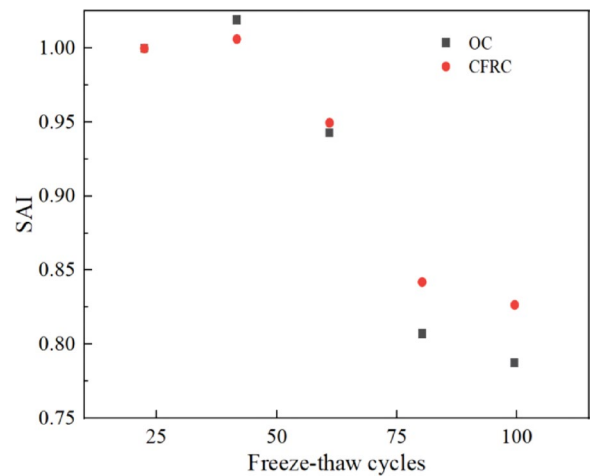**Fig. 9**. Static compressive strength of OC and CFRC under different freeze–thaw cycles.

Fig. 10. Changes of SAI under different freeze–thaw cycles.

Group	Formula	R²	Freezing–thawing cycles
OC	$SAI = 1.06 \times 10^{-6}n^3 - 1.72 \times 10^{-4}n^2 + 4.36 \times 10^{-3}n + 1.01$	0.991	[0,100]
CFRC	$SAI = 7.75 \times 10^{-7}n^3 - 1.24 \times 10^{-4}n^2 + 2.85 \times 10^{-3}n + 1.01$	0.997	[0,100]

Table 7. Correlation between SAI and freeze–thaw cycles (n).

In the equation, *SAI* represents the strength activity index of concrete specimens after *n* freezing–thawing cycles; f_n denotes the static compressive strength of concrete specimens after *n* freezing–thawing cycles, Mpa; f_0 represents the static compressive strength of concrete specimens before undergoing freezing–thawing cycles, Mpa.

Figure 10 is a scatter plot showing the relationship between the number of freezing–thawing cycles. From Fig. 8, it can be observed that the trend of the strength activity index with the number of freezing–thawing cycles is consistent with the trend of the static compressive strength with the number of freezing–thawing cycles. At 25, 50, 75, and 100 freezing–thawing cycles, the strength activity index of the OC specimens are 1.019, 0.943, 0.807, and 0.788 respectively, while the strength activity index of the CFRC specimens are 1.006, 0.950, 0.842, and 0.827 respectively.

In Fig. 10, an appropriate function was chosen to fit the strength activity index (*SAI*) of OC and CFRC specimens with the number of freezing–thawing cycles (n). In the chloride solution, the SAI of OC and CFRC specimens exhibited a cubic parabolic trend with the number of freezing–thawing cycles. The correlation coefficient (R²) after fitting was 0.967 for OC specimens and 0.977 for CFRC specimens. The specific fitting relationships are shown in Table 7. This indicates a strong linear correlation between the *SAI* of the specimens and the number of freezing–thawing cycles (*n*), validating the rationality of using the strength activity index to evaluate the mechanical properties of concrete specimens under the coupling effect of chloride salt and freezing–thawing cycles.

Stress–strain curve
Figure 11 and 12 depict the stress–strain curves of OC and CFRC specimens in chloride solution after 0, 25, 50, 75, and 100 freezing–thawing cycles, respectively.

From Figs. 11 and 12, it can be observed that after the chloride freezing–thawing cycle test, the stress–strain curves of OC and CFRC under uniaxial compression exhibit similar patterns. With an increase in the number of freezing–thawing cycles, the peak stress of both OC and CFRC specimens shows a decreasing trend, and the decrease in peak stress becomes more pronounced with an increasing number of freezing–thawing cycles. This is due to the formation of ice during the freezing–thawing process, as well as the action of the hydrostatic pressure, leading to the continuous development of cracks, an increase in crack width, and surface spalling, resulting in a decrease in specimen integrity. With a higher number of freezing–thawing cycles, there is an increase in internal erosion products within the specimen, more crystallization of chloride salt, and an increase in pore pressure.

(1) Peak strain

The peak strain corresponding to the peak stress in the stress–strain curve of concrete specimens can intuitively reflect the degree of damage to the concrete specimens. The peak strains of OC and CFRC under different freezing–thawing cycles in chloride environment are shown in Fig. 13.

From Fig. 13, it can be seen that with an increase in the number of freezing–thawing cycles, the peak strains of both OC and CFRC show an increasing trend. This trend becomes more pronounced especially after 75
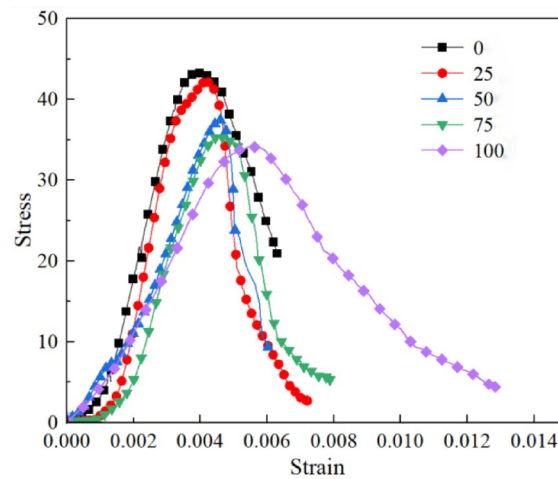
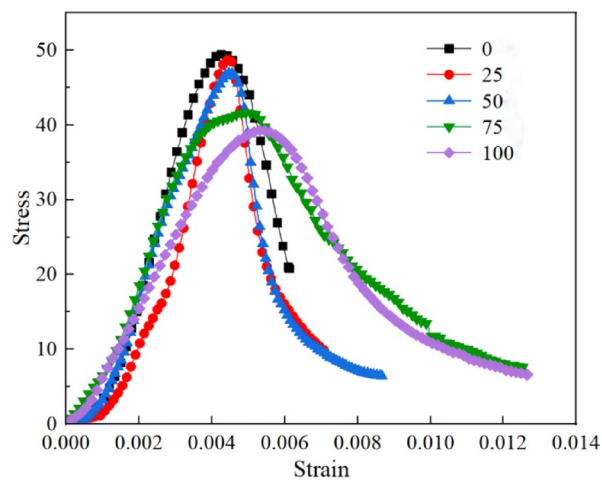**Fig. 11**. Stress–strain curves of OC under different freeze–thaw cycles.

Fig. 12. Stress–strain curves of CFRC under different freeze–thaw cycles.
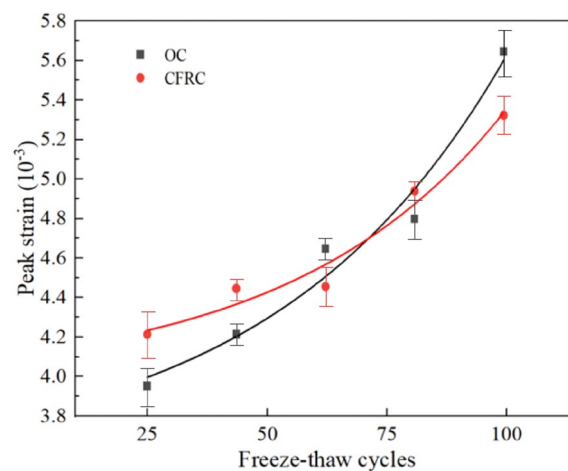

Fig. 13. Variation of peak strain under different freeze–thaw cycles.

freezing–thawing cycles. After 75 and 100 cycles, the peak strains of OC reach 1.21 times and 1.43 times the pre-freezing–thawing peak strain, respectively, while the peak strains of CFRC reach 1.17 times and 1.26 times the pre-freezing–thawing peak strain, respectively.

(2) Elastic modulus

The values of the elastic modulus in this paper are calculated based on the secant modulus corresponding to 40% of the peak stress. The changes in the elastic modulus of OC and CFRC under different freezing–thawing cycles in a chloride environment are shown in Fig. 14.

From Fig. 14, it can be observed that in a chloride environment, the elastic modulus of both OC and CFRC gradually decreases with an increase in the number of freezing–thawing cycles. In the figure, when the number of freezing–thawing cycles is the same, the elastic modulus of CFRC is consistently higher than that of OC. This is because with an increase in the number of freezing–thawing cycles, the combined action of chloride erosion products, chloride crystalline substances, and freeze–thaw cycles will cause the concrete specimens to crack, resulting in a decrease in specimen stiffness and a reduction in elastic modulus. However, with the addition of carbon fibers, it is possible to better connect the concrete specimen matrix, significantly improving the compactness of the specimen compared to OC, and thus increasing the elastic modulus.

The dynamic mechanical properties of carbon fiber reinforced concrete under the coupling effect of chloride salt and freeze–thaw cycles

Table 8 outlines the failure modes of OC and CFRC specimens under varying impact pressures after different freeze–thaw cycles. Specimens with fewer freeze–thaw cycles show more complete fragmentation, indicating that these cycles in chloride solution cause additional damage. At the same impact pressure, specimens without freeze–thaw cycles retain intact central regions, with block-like fragmentation at the edges. After 25 cycles, the central region's integrity improves, leading to increased edge fragmentation. At 50 cycles, the central region breaks into larger fragments, while fragmentation remains consistent for 75 and 100 cycles. The volume of fragments in the central region decreases, aligning more closely with edge fragmentation. When freeze–thaw cycles are fewer than 50, the central region fails more due to confinement from surrounding concrete. As cycles increase, the specimen's internal structure loosens, resulting in similar damage levels between central and edge regions.

Under the same number of freeze–thaw cycles, the extent of damage and fragmentation of both OC and CFRC increases with increasing impact pressure. At an impact pressure of 0.3 MPa, slight cracks and minor particle detachment occur at the edges of the specimens. At 0.4 MPa, the edges of the specimens break into small fragments while the central region remains intact. As the impact pressure increases to 0.5 MPa, the degree of damage in the central region gradually increases, with the size of the damage exceeding that of the edge. At 0.6 MPa, the size of the damage in the central region becomes close to that of the edge, and some of the edge damage changes to a powdery form. This is consistent with the aforementioned influence of the number of freeze–thaw cycles on the failure mode.

Stress–strain curve
Based on the calculation principles of the Split Hopkinson Pressure Bar (SHPB) tests[37,38], the specimen's stress (σ), strain (ε), and strain rate ($\dot{\varepsilon}$) can be calculated using Eq. (3). This yields the dynamic compression stress–strain data for OC and CFRC after different numbers of freeze–thaw cycles. From these data, the values closest to the peak stress are selected as the experimental results. Based on the selected data, dynamic compression stress–strain curves for OC and CFRC after different numbers of freeze–thaw cycles are plotted, as shown in Figs. 15 and 16.
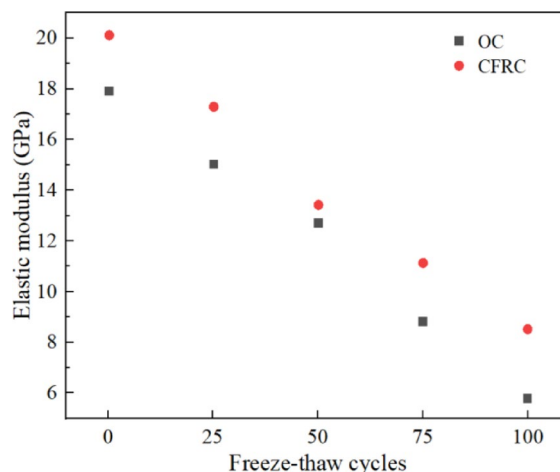

Fig. 14. Variation law of elastic modulus.
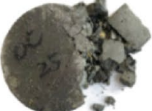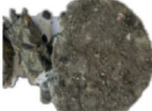
Freeze-thaw cycles	Group	0.3 MPa	0.4 MPa	0.5 MPa	0.6 MPa
0	OC				
	CFRC				
25	OC				
	CFRC				
50	OC				
	CFRC				
75	OC				
	CFRC				
100	OC				
	CFRC				

Table 8. Impact failure patterns of OC and CFRC under different freeze–thaw cycles.
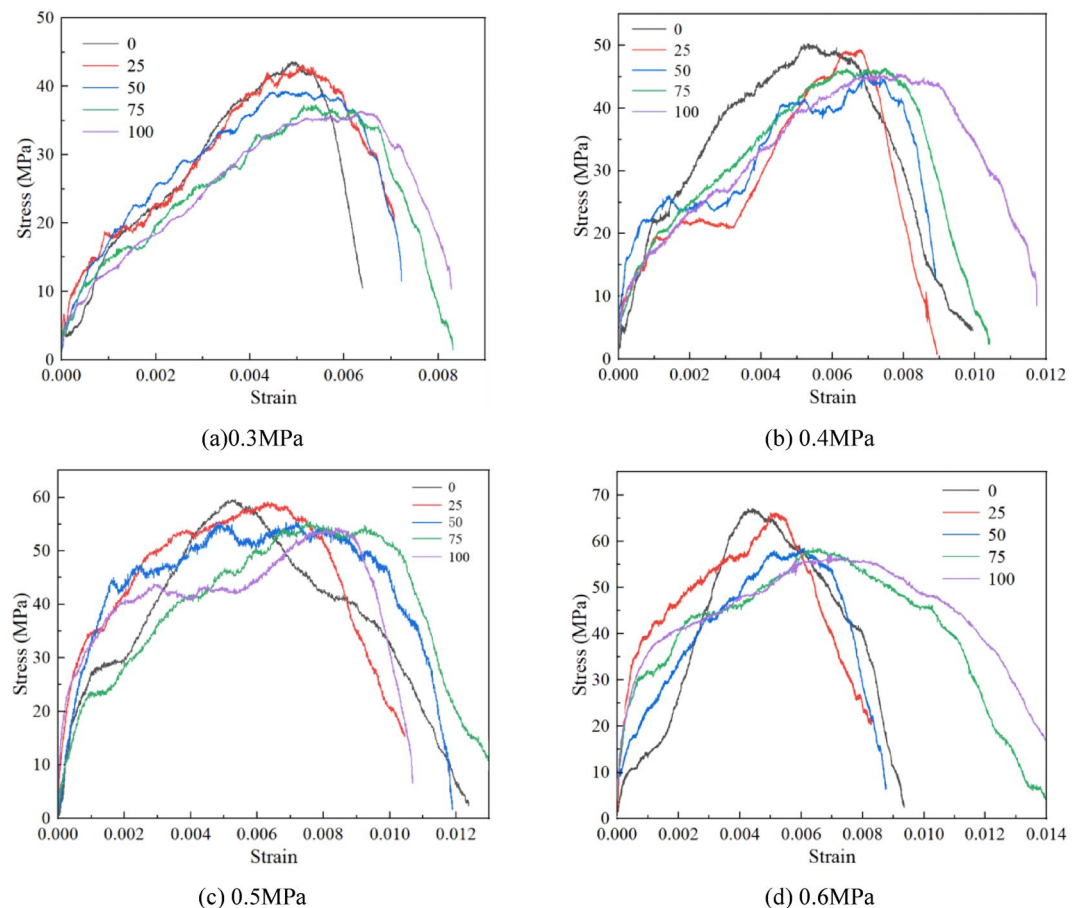
Fig. 15. Dynamic stress–strain curves of OC under different freeze–thaw cycles.

$$\begin{cases} \sigma(t) = \dfrac{EA}{2A_s}\left[\varepsilon_i(t) + \varepsilon_r(t) + \varepsilon_t(t)\right] \\[2mm] \varepsilon(t) = \dfrac{C_0}{L_S}\left[\varepsilon_i(t) - \varepsilon_r(t) - \varepsilon_t(t)\right] \\[2mm] \dot{\varepsilon}(t) = \dfrac{C_0}{L_S}\displaystyle\int\limits_0^t \left[\varepsilon_i(t) - \varepsilon_r(t) - \varepsilon_t(t)\right]dt \end{cases} \quad (3)$$

In the equation, $\varepsilon_i(t)$, $\varepsilon_r(t)$, and $\varepsilon_t(t)$ represent the incident strain, reflected strain, and transmitted strain in the pressure bar. E and C_0 represent the elastic modulus and wave velocity of the pressure bar, GPa and m/s, respectively. A and A_S represent the cross-sectional areas of the bar and the specimen, cm². L_S represents the thickness of the specimen, cm.

From Figs. 15 and 16, it can be observed that the dynamic stress–strain curves of OC and CFRC specimens exhibit similar trends with changes in the number of freeze–thaw cycles and strain rate. Initially, when the dynamic load is applied to the concrete specimen, the generated stress is relatively small, causing closure of inherent pores and small cracks within the specimen, leading to increased density and enhanced friction between aggregates, cement matrix, and fibers. This results in an overall increase in the elastic modulus of the specimen, leading to elastic deformation, thereby causing the stress–strain curve to exhibit an approximately linear relationship. As the loading time increases, the impact energy rises, leading to an increase in stress. When the friction between aggregates, cement matrix, and fibers within the specimen reaches its limit, the contact interface starts to slip, resulting in crack formation and significant deformation. It is noteworthy that due to the inclusion of carbon fibers in CFRC, the carbon fibers play a "bridging effect", connecting the matrix to restrain specimen deformation, hence the CFRC dynamic stress–strain curve exhibits a distinct plateau stage. When the stress applied to the concrete specimen reaches its maximum and the transition interface sliding between aggregates and the concrete matrix reaches its maximum, small pores and cracks expand and merge to form larger and more numerous cracks, causing the fiber bridging effect to fail, leading to a significant decrease in load-bearing capacity, ultimately resulting in specimen failure.

Upon comparing the graphs in Fig. 15 or Fig. 16, it is evident that under the same impact strain rate loading, the peak stress of OC decreases with an increase in the number of freeze–thaw cycles, while the peak stress of

(a) 0.3MPa

(b) 0.4MPa

(c) 0.5MPa

(d) 0.6MPa
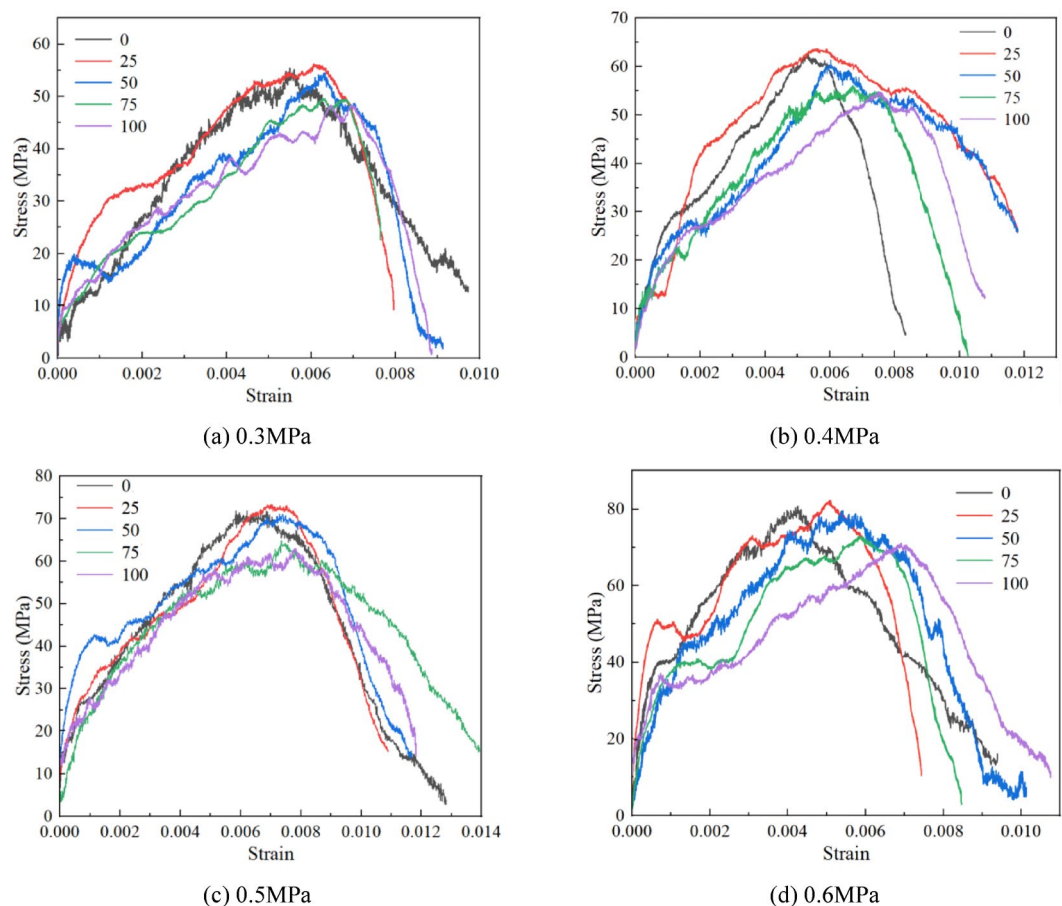
Fig. 16. Dynamic stress–strain curves of CFRC under different freeze–thaw cycles.

CFRC slightly increases as the number of freeze–thaw cycles goes from 0 to 25, consistent with the previous trend of static strength changes in CFRC. After 25 freeze–thaw cycles, the peak stress of CFRC gradually starts to decrease. The peak strain of both OC and CFRC gradually increases with the increase in the number of freeze–thaw cycles, resulting in a rightward shift of the curves. Furthermore, comparing Figs. 15 and 16 reveals that under the same number of freeze–thaw cycles, the peak stress and peak strain of both OC and CFRC increase with an increase in strain rate. Moreover, the peak stress of CFRC is consistently greater than that of OC, indicating that CFRC is more sensitive to strain rate effects.

Dynamic compressive strength
The above analysis mainly focused on the stress–strain curve variations of OC and CFRC specimens under impact loading after experiencing different freeze–thaw cycles, but did not specifically analyze the coupled effect of freeze–thaw cycles and strain rate on the dynamic mechanical properties of OC and CFRC. Therefore, based on Figs. 15, 16, and the experimental data, the test results are obtained as shown in Tables 9 and 10.

Dynamic strength variation law

(1)   The relationship between dynamic compressive strength and freeze–thaw cycles

The dynamic compressive strength of OC and CFRC under different freeze–thaw cycles is obtained from the data in Tables 9 and 10, as shown in Fig. 17.

Based on Tables 9 and 10, it can be observed that under different impact pressures, the dynamic compressive strength of OC decreases with an increasing number of freeze–thaw cycles, showing a significant decline compared to its strength without freeze–thaw treatment. In contrast, when the number of freeze–thaw cycles is 25, the dynamic compressive strength of CFRC shows a slight increase. However, beyond 25 cycles, the strength of CFRC also decreases with an increasing number of freeze–thaw cycles, ultimately falling below the strength of the untreated samples. Overall, the dynamic compressive strengths of OC and CFRC exhibit different trends under the influence of freeze–thaw cycles, with CFRC demonstrating greater strength than OC under the same conditions.

Based on the analysis of the fitting between the dynamic compressive strength of OC and CFRC with the number of freeze–thaw cycles, as shown in Fig. 18, it is found that there is a cubic function relationship between

Freeze–thaw cycles	Strain rate (s⁻¹)	Static compressive strength (MPa)	Peak stress (MPa)	Elastic modulus (GPa)	Dynamic increase factor
0	44.54	43.46	45.2	27.89	1.04
	64.08		49.98	34.47	1.15
	74.37		59.97	42.53	1.38
	106.97		67.36	49.37	1.55
25	43.81	42.3	43.99	25.12	1.05
	63.81		49.07	30.12	1.16
	73.89		59.22	37.30	1.40
	95.27		66.41	43.41	1.57
50	40.12	37.56	40.19	22.89	1.07
	64.49		46.95	27.48	1.25
	74.20		56.71	34.99	1.51
	111.92		60.85	38.22	1.62
75	45.06	35.39	38.22	19.16	1.08
	64.02		46.07	25.32	1.30
	71.75		55.56	29.52	1.57
	94.86		58.74	31.01	1.66
100	42.30	34.23	37.31	16.25	1.09
	62.92		45.18	19.68	1.32
	80.66		54.76	23.86	1.60
	95.27		57.50	27.59	1.68

Table 9. Dynamic compression test results of OC after different freeze–thaw cycles.

Freeze–thaw cycles	Strain rate (s⁻¹)	Static compressive strength (MPa)	Peak stress (MPa)	Elastic modulus (GPa)	Dynamic increase factor
0	45.71	49.98	55.48	30.01	1.11
	66.77		62.48	36.65	1.25
	75.52		70.47	43.85	1.41
	101.77		79.46	51.77	1.59
25	44.47	50.3	56.34	30.3	1.12
	59.56		63.88	37.73	1.27
	76.12		71.93	44.60	1.43
	103.24		80.98	52.28	1.61
50	39.48	47.47	54.59	25.58	1.15
	60.43		61.24	32.67	1.29
	73.53		69.78	40.49	1.47
	99.62		78.33	46.73	1.65
75	44.28	42.1	49.68	21.38	1.18
	65.27		55.99	26.59	1.33
	75.00		63.57	34.71	1.51
	96.86		71.99	42.44	1.71
100	45.67	40.73	48.46	18.87	1.19
	61.49		54.57	21.86	1.34
	80.19		61.90	26.80	1.53
	101.75		70.01	34.92	1.72

Table 10. Dynamic compression test results of CFRC after different freeze–thaw cycles.

the two. The specific fitting relationships are shown in Table 11. From Fig. 17 and Table 11, it can be seen that the correlation coefficients of each fitting relationship are all greater than 0.9, indicating a good fitting effect.

(2) Relationship between dynamic compressive strength and strain rate

Based on the data from Tables 9 and 10, the variations of dynamic compressive strength of OC and CFRC with strain rate are shown in Fig. 18.

From Fig. 18, it can be observed that under the same number of freeze–thaw cycles, the dynamic compressive strength of both OC and CFRC increases with the rise in strain rate. The improvement in the dynamic compressive strength of OC at different freeze–thaw cycles is as follows: approximately 10.58% to 49.03% without freeze–
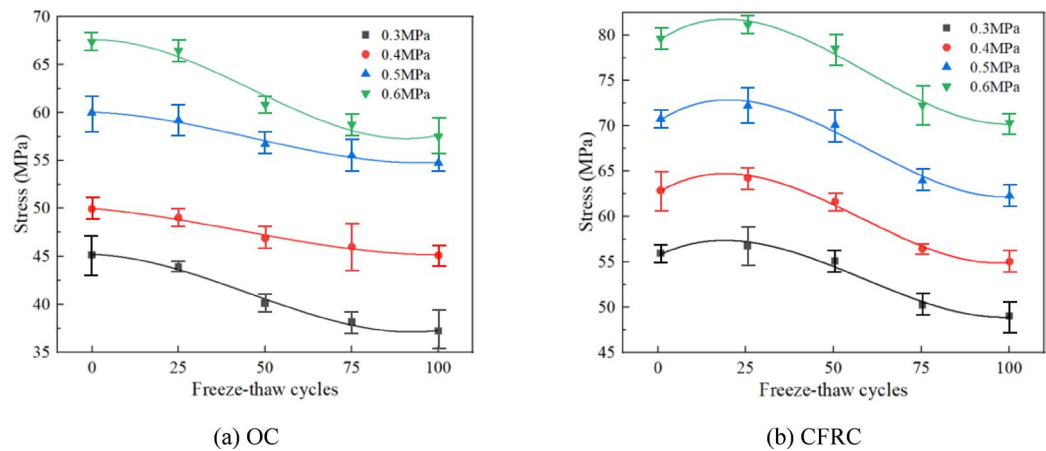
(a) OC (b) CFRC

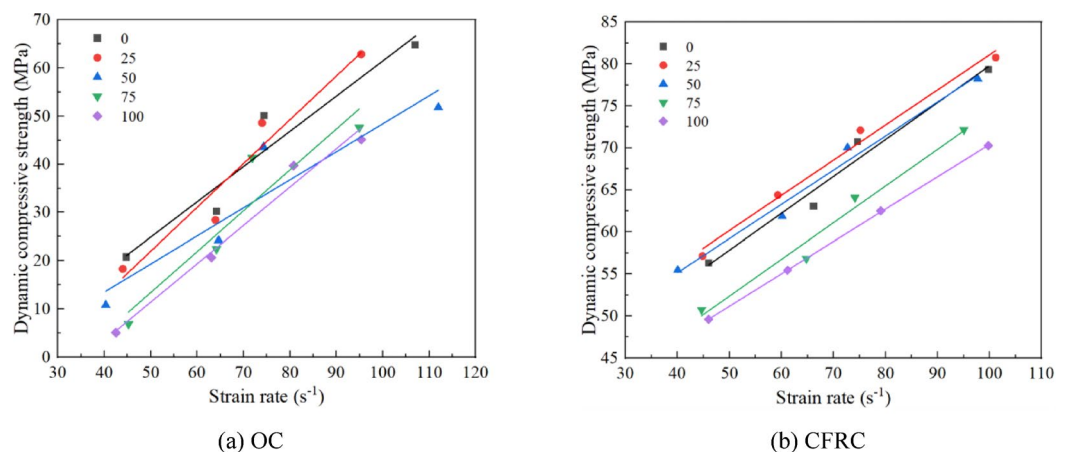**Fig. 17**. Relationship between stress and freeze–thaw cycles of OC and CFRC under different impact pressure.

(a) OC (b) CFRC

Fig. 18. Relationship between stress and strain rate of OC and CFRC.

Impact load (MPa)	Group	Fitting formula	R^2
0.3	OC	$\sigma_{oc} = 45.27 - 0.0093n - 0.0026n^2 + 1.95 \times 10^{-5}n^3$	0.968
	CFRC	$\sigma_{CFRC} = 55.39 + 0.1815n - 0.0059n^2 + 3.36 \times 10^{-5}n^3$	0.939
0.4	OC	$\sigma_{oc} = 50.03 - 0.0306n - 8.1 \times 10^{-4}n^2 + 6.4 \times 10^{-6}n^3$	0.952
	CFRC	$\sigma_{CFRC} = 62.41 + 0.2251n - 0.0072n^2 + 4.2 \times 10^{-5}n^3$	0.979
0.5	OC	$\sigma_{oc} = 60.03 - 0.0102n - 0.0015n^2 + 1.13 \times 10^{-5}n^3$	0.953
	CFRC	$\sigma_{CFRC} = 70.34 + 0.2496n - 0.0077n^2 + 4.35 \times 10^{-5}n^3$	0.942
0.6	OC	$\sigma_{oc} = 67.51 - 0.0147n - 0.0041n^2 + 2.92 \times 10^{-5}n^3$	0.919
	CFRC	$\sigma_{CFRC} = 79.35 + 0.2551n - 0.0081n^2 + 4.55 \times 10^{-5}n^3$	0.965

Table 11. Fitting relationship between dynamic compressive strength and freeze–thaw cycles of OC and CFRC.

thaw treatment, about 11.55% to 50.96% after 25 cycles, around 16.82% to 51.41% after 50 cycles; approximately 20.54% to 53.69% after 75 cycles, and about 21.09% to 54.11% after 100 cycles. Similarly, the dynamic compressive strength of CFRC shows a comparable trend across different freeze–thaw cycles: an increase of about 12.62% to 43.22% without freeze–thaw treatment; approximately 12.60% to 43.73% after 25 cycles; about 12.18% to 43.49% after 50 cycles; approximately 12.70% to 44.91% after 75 cycles; and around 12.61% to 44.47% after 100 cycles. Overall, both OC and CFRC exhibit a significant increase in dynamic compressive strength influenced by the strain rate, demonstrating a pronounced strain rate enhancement effect.

Freeze–thaw cycles	OC	R^2	CFRC	R^2
0	$\sigma_{oc} = 0.368\dot{\varepsilon} + 28.97$	0.90	$\sigma_{CFRC} = 0.439\dot{\varepsilon} + 35.17$	0.96
25	$\sigma_{oc} = 0.457\dot{\varepsilon} + 23.04$	0.91	$\sigma_{CFRC} = 0.418\dot{\varepsilon} + 38.63$	0.98
50	$\sigma_{oc} = 0.292\dot{\varepsilon} + 29.93$	0.87	$\sigma_{CFRC} = 0.406\dot{\varepsilon} + 38.25$	0.97
75	$\sigma_{oc} = 0.426\dot{\varepsilon} + 20.29$	0.88	$\sigma_{CFRC} = 0.436\dot{\varepsilon} + 29.61$	0.96
100	$\sigma_{oc} = 0.400\dot{\varepsilon} + 20.59$	0.97	$\sigma_{CFRC} = 0.385\dot{\varepsilon} + 30.92$	0.99

Table 12. Fitting relationship between dynamic compressive strength and strain rate of OC and CFRC.
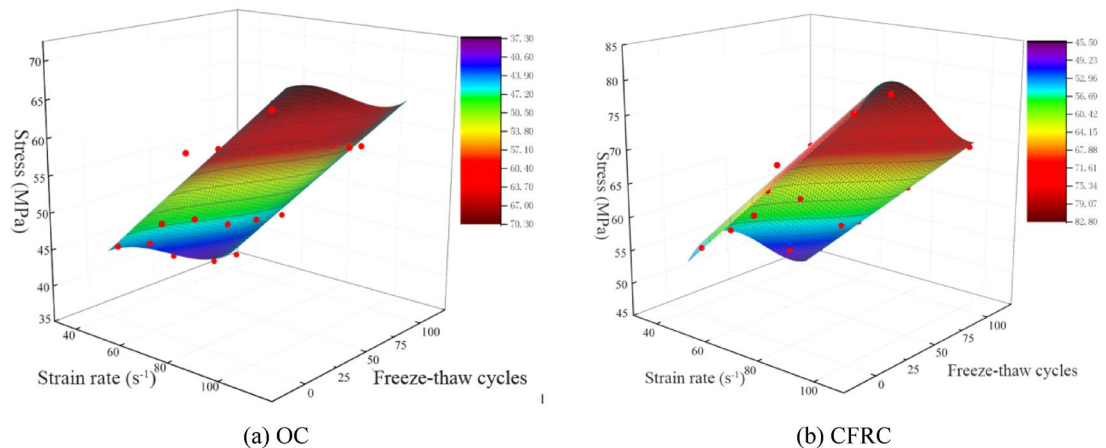

(a) OC (b) CFRC

Fig. 19. Fitting relationship among dynamic compressive strength, strain rate and number of freeze–thaw cycles.

Fitting analysis of the dynamic compressive strength of OC and CFRC with strain rate revealed a nearly linear relationship, as shown in Table 12. The correlation coefficients (R^2) of the fitting relationships were all higher than 0.85, indicating a good fitting effect.

(3) Relationship between dynamic compressive strength, strain rate and freeze–thaw cycles

Based on the experimental results and the relationships in the previous two sections, a surface fitting analysis was conducted for the dynamic compressive strength, strain rate, and number of freeze–thaw cycles of OC and CFRC. The fitting surface plots are shown in Fig. 19, with fitting correlation coefficients (R^2) of 0.864 and 0.974 respectively, indicating a good fitting effect. The surface fitting relationships are as follows:

$$\sigma_{OC} = 29.684 + 0.362 \times \dot{\varepsilon} - 0.002 \times n - 0.002 \times n^2$$
$$+1.77 \times 10^{-5} n^3 + 1.74 \times 10^{-4} n\dot{\varepsilon} \tag{4}$$

$$\sigma_{CFRC} = 35.395 + 0.434 \times \dot{\varepsilon} - 0.304 \times n - 0.008 \times n^2$$
$$+3.97 \times 10^{-5} n^3 - 3.78 \times 10^{-4} n\dot{\varepsilon} \tag{5}$$

<u>Dynamic increase factor</u>   To quantify the effect of strain rate on the dynamic compressive strength of concrete specimens, many scholars use the dynamic increase factor (DIF), which is the ratio of dynamic compressive strength to static compressive strength, to measure it[39,40]. The variation of DIF with strain rate under different freeze–thaw cycles for OC and CFRC is shown in Fig. 20.

According to Fig. 20, both OC and CFRC exhibit an increasing trend in DIF as the strain rate rises. For OC, the range of DIF increase without freeze–thaw cycles is approximately 10.5% to 49.0%. When subjected to 25, 50, 75, and 100 freeze–thaw cycles, the ranges of DIF increase for OC are approximately 10.5% to 49.5%, 16.8% to 51.4%, 20.4% to 53.7%, and 21.1% to 54.1%, respectively. This indicates that the magnitude of DIF growth also increases with the number of freeze–thaw cycles.

In the case of CFRC, the range of DIF increase without freeze–thaw cycles is approximately 12.6% to 43.2%. For 25, 50, 75, and 100 freeze–thaw cycles, the ranges of DIF increase are approximately 13.4% to 43.8%, 12.2% to 43.5%, 12.7% to 44.9%, and 12.6% to 44.6%, respectively. Notably, the DIF of CFRC consistently remains higher than that of OC, further confirming the strain rate enhancement effect observed in both OC and CFRC, with CFRC showing greater sensitivity to changes in strain rate.

The study observed that the increase in the dynamic increase factor (DIF) with strain rate arises from the synergistic effects of multiple mechanisms, including the enhanced stiffness due to the viscoelastic response of the
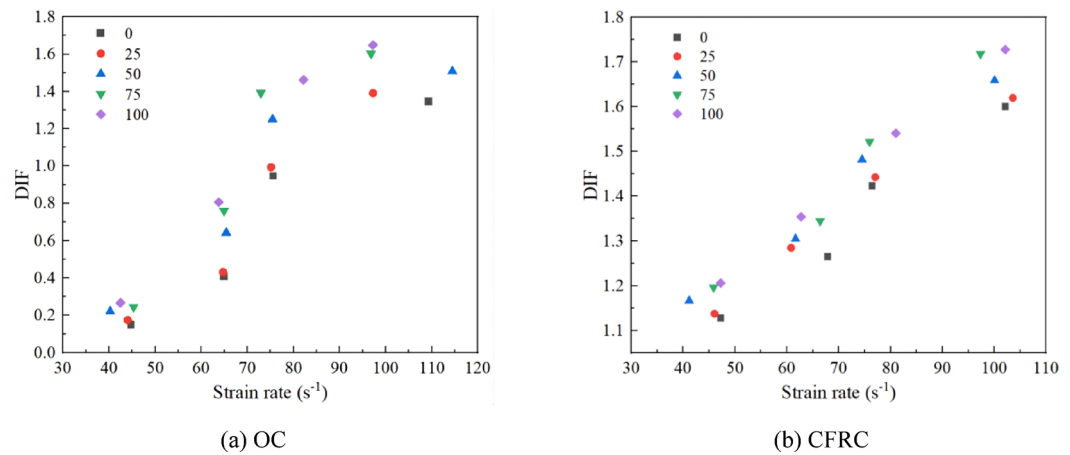
(a) OC

(b) CFRC

Fig. 20. The variation of DIF with strain rate.
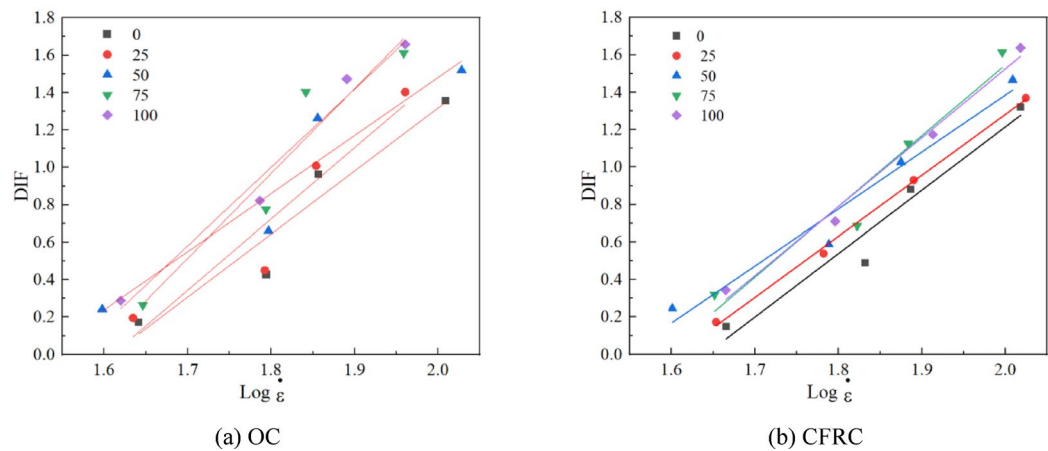

(a) OC

(b) CFRC

Fig. 21. Logarithmic fitting of DIF with strain rate.

cement matrix, the closure of microcracks under dynamic compression leading to improved apparent strength, and the delay in material failure caused by inertial effects at high strain rates. In carbon fiber-reinforced concrete (CFRC), the bridging effect of the fibers effectively suppresses crack propagation, resulting in a consistently higher DIF compared to ordinary concrete (OC). Comparison of experimental data with the CEB-FIP model revealed that ordinary concrete conforms to the model predictions in the low strain rate range, whereas carbon fiber-reinforced concrete consistently exhibits superior dynamic enhancement, validating the positive effect of fiber reinforcement. After freeze–thaw cycles, the degradation of the DIF in ordinary concrete was significantly greater than that in carbon fiber-reinforced concrete, further confirming the role of carbon fibers in enhancing the durability of concrete under harsh environmental conditions.

Since Fig. 20 cannot visually express the relationship between strain rate and DIF, in order to further analyze the relationship between strain rate and DIF, a linear fitting analysis is carried out using the near-linear fitting relationship between the dynamic increase factor proposed by Tedesco and the logarithm of the average strain rate. The relationship is expressed as follows:

$$DIF = k \log \dot{\varepsilon} + b \tag{6}$$

In the equation, k and b are both fitting parameters.

The DIF of OC and CFRC with strain rate is fitted according to the linear relationship in Eq. (6), and the fitting relationship graph is shown in Fig. 21. The specific fitting functions are presented in Table 13, with R-squared values greater than 0.9, indicating a good fitting effect.

<u>Elastic modulus</u>   The method proposed by Xiao[41] is used to calculate the elastic modulus, which determines the elastic modulus using the slope of the stress–strain curve between 40 and 60% of the dynamic compressive strength. The calculation formula is as follows:

$$E = (\sigma_2 - \sigma_1)/(\varepsilon_2 - \varepsilon_1) \tag{7}$$

Freeze–thaw cycles	OC	R²	CFRC	R²
0	$DIF_{OC} = 1.403 \log \dot{\varepsilon} - 1.299$	0.93	$DIF_{CFRC} = 1.405 \log \dot{\varepsilon} - 1.25$	0.93
25	$DIF_{OC} = 1.586 \log \dot{\varepsilon} - 1.596$	0.91	$DIF_{CFRC} = 1.353 \log \dot{\varepsilon} - 1.117$	0.99
50	$DIF_{OC} = 1.292 \log \dot{\varepsilon} - 1.007$	0.91	$DIF_{CFRC} = 1.264 \log \dot{\varepsilon} - 0.899$	0.96
75	$DIF_{OC} = 1.888 \log \dot{\varepsilon} - 2.04$	0.92	$DIF_{CFRC} = 1.569 \log \dot{\varepsilon} - 1.439$	0.92
100	$DIF_{OC} = 1.743 \log \dot{\varepsilon} - 1.763$	0.97	$DIF_{CFRC} = 1.528 \log \dot{\varepsilon} - 1.367$	0.98

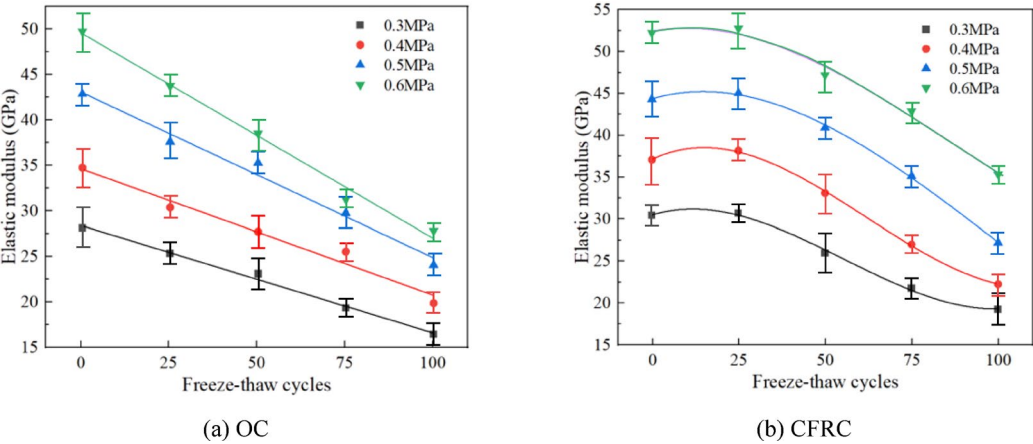**Table 13**. Fitting relationship between DIF and strain rate of OC and CFRC.

(a) OC   (b) CFRC

Fig. 22. Variation of elastic modulus with freeze–thaw cycles under different impact pressures.

In the equation, σ_2 and σ_1 represent the 60% dynamic compressive strength and 40% dynamic compressive strength respectively, while ε_2 and ε_1 represent the strains corresponding to the 60% dynamic compressive strength and 40% dynamic compressive strength respectively.

(1) The relationship between elastic modulus and freeze–thaw cycles

Based on the data in Tables 10 and 11, the relationship between the elastic modulus of OC and CFRC in chloride solution and the number of freeze–thaw cycles can be seen in Fig. 22.

According to Fig. 22a, under the same impact pressure, the elastic modulus of OC shows a decreasing trend as the number of freeze–thaw cycles increases. Specifically, at an impact pressure of 0.3 MPa, the elastic modulus of OC decreases by approximately 9.9% to 41.7%; at 0.4 MPa, the decrease ranges from about 12.6% to 42.9%; at 0.5 MPa, it decreases by approximately 12.3% to 43.9%; and at 0.6 MPa, the reduction is about 12.1% to 44.1%. Figure 22b illustrates that the elastic modulus of CFRC initially increases and then decreases as the number of freeze–thaw cycles increases. When the number of freeze–thaw cycles reaches 25, the elastic modulus of CFRC shows a slight increase compared to the uncycled state, with an increase ranging from approximately 0.97% to 2.95% across different pressures. Once the number of freeze–thaw cycles exceeds 25, at 0.3 MPa, the elastic modulus of CFRC decreases by approximately 14.8% to 37.1%; at 0.4 MPa, the decrease is about 10.9% to 40.4%; at 0.5 MPa, it reduces by approximately 7.7% to 38.9%; and at 0.6 MPa, the reduction is around 9.7% to 32.6%.

In summary, a comparison of the two figures reveals that at lower impact pressures, the effect of carbon fiber on the elastic modulus of concrete specimens is relatively minor. However, at higher impact pressures, the reduction in the elastic modulus of CFRC is significantly less than that of OC, indicating that carbon fiber significantly mitigates damage to CFRC specimens in chloride salt freeze–thaw environments.

The relationship between the elastic modulus of OC and CFRC and the number of freeze–thaw cycles, a fitting analysis was conducted, revealing that the elastic modulus of OC shows an approximate linear relationship with the number of freeze–thaw cycles, with fitting correlation coefficients (R^2) all exceeding 0.9. The elastic modulus of CFRC demonstrates a cubic function relationship with the number of freeze–thaw cycles, also with fitting correlation coefficients (R^2) all exceeding 0.9. The specific fitting functions are detailed in Table 14.

(2) The relationship between elastic modulus and strain rate

The relationship between the elastic modulus and strain rate of OC and CFRC in chloride environments is shown in Fig. 23.

According to Fig. 23, the elastic modulus of both OC and CFRC increases with the rise in loading strain rate across different freeze–thaw cycle counts, demonstrating a significant strain rate enhancement effect. In the absence of freeze–thaw cycles in a chloride salt environment, the elastic modulus of OC increases by

Impact load (MPa)	Fitting formula	R^2
0.3	$E_{OC} = -0.117n + 28.11$	0.992
	$E_{CFRC} = 30.07 + 0.1253n - 0.0059n^2 + 3.57 \times 10^{-5}n^3$	0.990
0.4	$E_{OC} = -0.138n + 34.29$	0.966
	$E_{CFRC} = 36.69 + 0.1963n - 0.0074n^2 + 3.99 \times 10^{-5}n^3$	0.998
0.5	$E_{OC} = -0.18n + 42.66$	0.979
	$E_{CFRC} = 43.9 + 0.1193n - 0.0044n^2 + 1.46 \times 10^{-5}n^3$	0.997
0.6	$E_{OC} = -0.224n + 49.11$	0.989
	$E_{CFRC} = 51.94 + 0.0761n - 0.004n^2 + 1.51 \times 10^{-5}n^3$	0.962

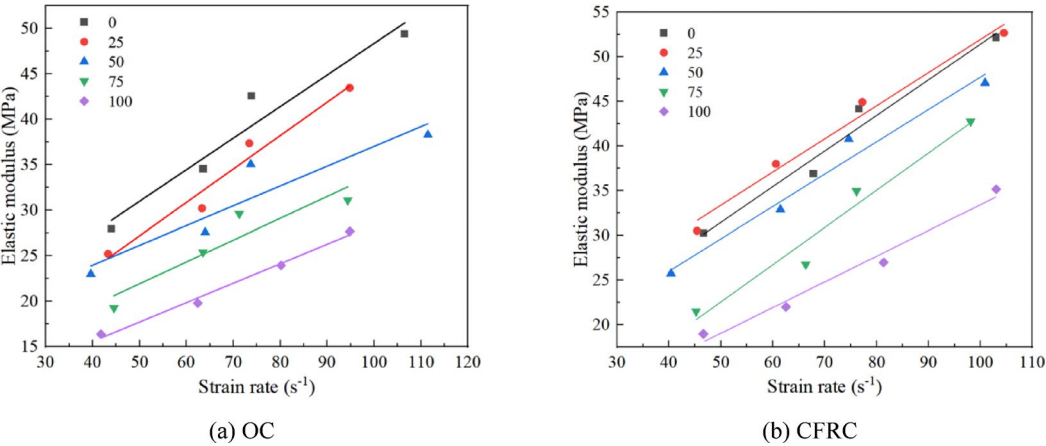**Table 14.** Fitting function relationship between elastic modulus and freeze–thaw cycles(n) under different impact pressure.

(a) OC (b) CFRC

Fig. 23. Relationship between elastic modulus and strain rate under different freeze–thaw cycles.

Freeze–thaw cycles	OC	R^2	CFRC	R^2
0	$E_{OC} = 0.349\dot{\varepsilon} + 13.289$	0.92	$E_{CFRC} = 0.398\dot{\varepsilon} + 11.748$	0.96
25	$E_{OC} = 0.349\dot{\varepsilon} + 8.471$	0.95	$E_{CFRC} = 0.37\dot{\varepsilon} + 14.99$	0.97
50	$E_{OC} = 0.370\dot{\varepsilon} + 8.471$	0.87	$E_{CFRC} = 0.361\dot{\varepsilon} + 11.727$	0.96
75	$E_{OC} = 0.218\dot{\varepsilon} + 15.04$	0.87	$E_{CFRC} = 0.415\dot{\varepsilon} + 2.067$	0.94
100	$E_{OC} = 0.215\dot{\varepsilon} + 6.753$	0.98	$E_{CFRC} = 0.287\dot{\varepsilon} + 4.88$	0.98

Table 15. Fitting relationship between elastic modulus and strain rate.

approximately 23.6% to 77.0% as the loading strain rate increases. When subjected to 25 freeze–thaw cycles, the increase ranges from about 19.9% to 72.8%; at 50 cycles, it increases by approximately 20.1% to 66.9%; at 75 cycles, the increase is around 32.2% to 61.9%; and at 100 cycles, it rises by about 21.1% to 69.8%.

For CFRC, in the absence of freeze–thaw cycles in a chloride salt environment, the elastic modulus increases by approximately 22.1% to 72.5% with the rise in loading strain rate. After 25 freeze–thaw cycles, the increase is about 24.5% to 72.5%; at 50 cycles, it increases by approximately 27.7% to 82.7%; at 75 cycles, the increase ranges from about 24.4% to 98.5%; and at 100 cycles, it rises by approximately 15.9% to 85.1%. A comparison of Fig. 23a reveals that after 50 freeze–thaw cycles, the increase in the elastic modulus of CFRC at high strain rates is greater than that of OC.

Based on the relationship between elastic modulus and strain rate shown in Fig. 23, it is evident that there is a distinct nearly linear correlation between the two. A linear regression analysis was conducted on both datasets, revealing that the correlation coefficients (R^2) for OC and CFRC are both above 0.85. The specific fitting relationships are presented in Table 15.

(3) The relationship between elastic modulus, strain rate and freeze–thaw cycles

The discussions and analyses above indicate that the elastic modulus of OC and CFRC is influenced by both strain rate and the number of freeze–thaw cycles. To further understand the interplay between strain rate
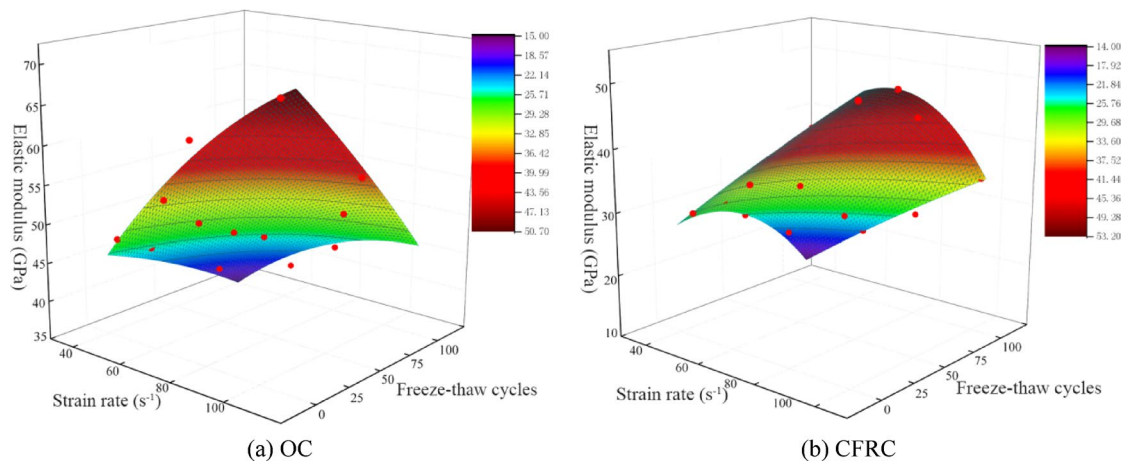
Fig. 24. Fitting relationship among elastic modulus, strain rate and number of freeze–thaw cycles.

and freeze–thaw cycles on the elastic modulus of OC and CFRC, surface fitting was performed based on the experimental results and the aforementioned fitting relationships. The correlation coefficients (R^2) for all three parameters are above 0.95. The fitting equations for the elastic modulus of OC and CFRC are presented in Eqs. (8) and (9), with the specific fitting results illustrated in Fig. 24.

$$\sigma_{OC} = 1.743 + 0.678 \times \dot{\varepsilon} - 6.668E - 5 \times n - 0.002 \times \dot{\varepsilon}^2$$
$$-2.985E - 4 \times n^2 - 0.002 \times n \times \dot{\varepsilon} \tag{8}$$

$$\sigma_{CFRC} = 9.455 + 0.478 \times \dot{\varepsilon} - 0.092 \times n - 5.286E - 4$$
$$\times \dot{\varepsilon}^2 - 0.002 \times n^2 - 7.441E - 4 \times n \times \dot{\varepsilon} \tag{9}$$

Conclusion

In this study, different dosages of carbon fiber-reinforced concrete were prepared to determine the optimal mix with the best performance. The dynamic and static mechanical properties of carbon fiber-reinforced concrete were investigated under chloride salt and freeze–thaw cycling conditions. By comparing the variations in mass, strength, and elastic modulus of the carbon fiber reinforced concrete, the stress–strain relationship was analyzed in conjunction with failure modes. This research explored the degradation mechanisms of the dynamic and static mechanical properties of carbon fiber-reinforced concrete under the coupled effects of chloride salt and freeze–thaw cycles, revealing the damage characteristics associated with the interaction between freeze–thaw cycles and strain rate. Nevertheless, this research lacks comprehensive validation of the fiber-matrix interface effects at a microstructural scale and did not include long-term field trials under real environmental conditions. Subsequent investigations will integrate microscopic analysis with field exposure tests to address these aspects. The study yielded the following main conclusions:

At a carbon fiber content of 0.4%, the static compressive strength and splitting tensile strength of concrete reached their maximum values of 49.98 MPa and 6.15 MPa, respectively, representing increases of 15.02% and 51.12% compared to ordinary concrete.

As the number of freeze–thaw cycles increased, the mass loss rate of carbon fiber-reinforced concrete remained consistently lower than that of ordinary concrete, with less surface damage. This indicates that carbon fibers effectively resist degradation caused by the combined effects of chloride salt and freeze–thaw cycles.

The dynamic compressive strength of carbon fiber-reinforced concrete increased with strain rate and consistently exceeded that of ordinary concrete, demonstrating a significant strain rate effect. The incorporation of carbon fibers mitigated freeze–thaw damage and improved the impact resistance of the concrete.

Under high strain rates, the decrease in the elastic modulus of carbon fiber-reinforced concrete was significantly smaller than that of ordinary concrete, whereas the effect of carbon fibers on the elastic modulus was relatively minor at low strain rates. This highlights the ability of carbon fibers to maintain material stiffness under high-strain conditions.

Data availability
Data will be provided by corresponding author on reasonable request.

References
1. Qu, F. et al. Phase transformation and microstructure of in-situ concrete after 20-year exposure to harsh mining environment: A case study. *Case. Stud. Constr. Mat.* **19**, e02287 (2023).

2. Wu, H.-L., Zhang, D., Du, Y.-J. & Li, V. C. Durability of engineered cementitious composite exposed to acid mine drainage. *Cem. Concr. Compos.* **108**, 103550 (2020).
3. Metalssi, O. O. et al. Understanding the degradation mechanisms of cement-based systems in combined chloride-sulfate attack. *Cem. Concr. Res.* **164**, 107065 (2023).
4. Shaheen, F. & Pradhan, B. Role of chloride ion and cation type accompanied by sulfate ion on durability performance of concrete in conjoint chloride–sulfate environment. *J. Mater. Civ. Eng.* **32**, 4020264 (2020).
5. Kim, J., Ryu, J. & Hooton, R. D. Evaluation of strength and set behavior of mortar containing shotcrete set accelerators. *Can. J. Civ. Eng.* **35**, 400–407 (2008).
6. Farnam, Y. et al. Performance of carbonated calcium silicate based cement pastes and mortars exposed to NaCl and $MgCl_2$ deicing salt. *Constr. Build. Mater.* **111**, 63–71 (2016).
7. Liu, Q. et al. Numerical study of interactive ingress of calcium leaching, chloride transport and multi-ions coupling in concrete. *Cem. Concr. Res.* **165**, 107072 (2023).
8. Zhao, G. et al. Degradation mechanisms of chloride contaminated cast-in-situ concrete partially exposed to magnesium-sulfate combined environment. *KSCE J. Civ. Eng.* **27**, 618–629 (2023).
9. Suryavanshi, A. K., Scantlebury, J. D. & Lyon, S. B. Mechanism of Friedel's salt formation in cements rich in tri-calcium aluminate. *Cem. Concr. Res.* **26**, 717–727 (1996).
10. Chen, S. et al. Investigation of the dynamic compressive mechanical properties of concrete under the combined effects of freeze–thaw and salt erosion. *Constr. Build. Mater.* **407**, 133548 (2023).
11. Cefis, N. & Comi, C. Chemo-mechanical modelling of the external sulfate attack in concrete. *Cem. Concr. Res.* **93**, 57–70 (2017).
12. Chung, C.-W., Shon, C.-S. & Kim, Y.-S. Chloride ion diffusivity of fly ash and silica fume concretes exposed to freeze–thaw cycles. *Constr. Build. Mater.* **24**, 1739–1745 (2010).
13. Qiu, J. et al. Deterioration characteristics of coal gangue concrete under the combined action of cyclic loading and freeze-thaw cycles. *J. Build. Eng.* **60**, 105165 (2022).
14. Jiang, W., Shen, X., Hong, S., Wu, Z. & Liu, Q. Binding capacity and diffusivity of concrete subjected to freeze-thaw and chloride attack: A numerical study. *Ocean Eng.* **186**, 106093 (2019).
15. Li, Y. et al. Dynamic mechanical properties and visco-elastic damage constitutive model of freeze–thawed concrete. *Materials* **13**, 4056 (2020).
16. Li, D., Li, L., Li, P. & Wang, Y. Modelling of convection, diffusion and binding of chlorides in concrete during wetting-drying cycles. *Mar. struct.* **84**, 103240 (2022).
17. Sotiriadis, K., Nikolopoulou, E. & Tsivilis, S. Sulfate resistance of limestone cement concrete exposed to combined chloride and sulfate environment at low temperature. *Cem. Concr. Compos.* **34**, 903–910 (2012).
18. Sotiriadis, K. et al. The effect of chlorides on the thaumasite form of sulfate attack of limestone cement concrete containing mineral admixtures at low temperature. *Constr. Build. Mater.* **43**, 156–164 (2013).
19. Pillay, D. L. et al. A review of the engineering properties of metakaolin based concrete: Towards combatting chloride attack in coastal/marine structures. *Adv. Civ. Eng.* **2020**, 8880974 (2020).
20. Zhang, B., Yan, B. & Li, Y. Study on mechanical properties, freeze–thaw and chlorides penetration resistance of alkali activated granulated blast furnace slag-coal gangue concrete and its mechanism. *Constr. Build. Mater.* **366**, 130218 (2023).
21. Al-Hadithi, A. I. & Hilal, N. N. The possibility of enhancing some properties of self-compacting concrete by adding waste plastic fibers. *J. Build. Eng.* **8**, 20–28 (2016).
22. Sotiriadis, K. et al. The effect of chlorides on the thaumasite form of sulfate attack of limestone cement concrete containing mineral admixtures at low temperature. *Constr. Bulid. Mater.* **43**, 156–164 (2013).
23. Feo, L., Ascione, F., Penna, R., Lau, D. & Lamberti, M. An experimental investigation on freezing and thawing durability of high performance fiber reinforced concrete (HPFRC). *Compos. Struct.* **234**, 111673 (2020).
24. Fu, Q., Xu, W., Bu, M., Guo, B. & Niu, D. Orthogonal experimental study on hybrid-fiber high-durability concrete for marine environment. *J. Mater. Res. Technol.* **13**, 1790–1804 (2021).
25. Chalah, L. & Talah, A. Permeability of high-performance fiber reinforced concrete immersed in high concentration sodium chloride solution. *Period. Polytech. Civ. Eng.* **66**, 541–552 (2022).
26. Liu, X. et al. Mechanical relationship between compressive strength and sulfate erosion depth of basalt fiber reinforced concrete. *Constr. Build. Mater.* **411**, 134412 (2024).
27. Khanzadeh Moradllo, M., Shekarchi, M. & Hoseini, M. Time-dependent performance of concrete surface coatings in tidal zone of marine environment. *Constr. Build. Mater.* **30**, 198–205 (2012).
28. Schueremans, L., Van Gemert, D. & Giessler, S. Chloride penetration in RC-structures in marine environment – long term assessment of a preventive hydrophobic treatment. *Constr. Build. Mater.* **21**, 1238–1249 (2007).
29. Kavitha, S. & Ravikumar, M. S. Behaviour of carbon and basalt fiber reinforced concrete under split tensile and flexural strength testing. *Adv. Concr. Constr.* **18**, 21–30 (2024).
30. Deng, Z. C. The fracture and fatigue performance in flexure of carbon fiber reinforced concrete. *Cem. Concr. Compos.* **27**, 131–140 (2005).
31. Wei, A., Tan, M. Y., Koay, Y.-C., Hu, X. & Al-Ameri, R. Effect of carbon fiber waste on steel corrosion of reinforced concrete structures exposed to the marine environment. *J. Clean. Prod.* **316**, 128356 (2021).
32. Li, Y.-F. et al. Comparing mechanical characterization of carbon, kevlar, and hybrid-fiber-reinforced concrete under quasistatic and dynamic loadings. *Buildings* **13**, 2044 (2023).
33. P.R.O.C. *Urban, Standard for Test Methods of Concrete Physical and Mechanical Properties* (2019).
34. C.A.B.R. *Standard for Test Methods of Long-term Performance and Durability of Ordinary Concrete* (China Architecture & Building Press, 2009).
35. Li, R., Zhu, J., Qu, H., Zhou, T. & Zhou, C. An experimental investigation on fatigue characteristics of granite under repeated dynamic tensions. *Int. J. Rock Mech. Min. Sci.* **158**, 105185 (2022).
36. Wang, J. & Zhang, J. Research on high-power and high-speed hydraulic impact testing machine for mine anti-impact support equipment. *Shock. Vib.* **2019**, 6545980 (2019).
37. Yu, L. et al. Dynamic fracturing properties of marble after being subjected to multiple impact loadings. *Eng. Fract. Mech.* **230**, 106988 (2020).
38. Li, M., Hao, H., Shi, Y. & Hao, Y. Specimen shape and size effects on the concrete compressive strength under static and dynamic tests. *Constr. Build. Mater.* **161**, 84–93 (2018).
39. Xiao, J., Li, Z., Xie, Q. & Shen, L. Effect of strain rate on compressive behaviour of high-strength concrete after exposure to elevated temperatures. *Fire Saf. J.* **83**, 25–37 (2016).
40. Yan, Z., Wu, W., Dai, F. & Liu, Y. Dynamic mechanical response and damage constitutive model of multi-flawed rocks under high strain rates. *Rock. Mech. Rock Eng.* **56**, 4405–4425 (2023).
41. Guo, Q., Gou, Y., Chen, J., Zhang, Y. & Zhou, Y. Dynamic response of foam concrete under low-velocity impact: Experiments and numerical simulation. *Int. J. Impact Eng.* **146**, 103693 (2020).

Author contributions

G.T.: Conceptualization, Investigation, Formal analysis, Visualization, Writing-original draft. J.X.: Funding ac-

quisition, Project administration, Supervision, Writing-review & editing. Z.S.: Software, Investigation, Methodology, Data curation. J.P.: Formal analysis, Validation. R.Z.: Resources, Visualization.

Declarations

Competing interests
The authors declare no competing interests.

Additional information
Correspondence and requests for materials should be addressed to G.T.

Reprints and permissions information is available at www.nature.com/reprints.

Publisher's note Springer Nature remains neutral with regard to jurisdictional claims in published maps and institutional affiliations.